Agricultural Water Management 306 (2024) 109207

Contents lists available at ScienceDirect

Agricultural Water Management

journal homepage: www.elsevier.com/locate/agwat

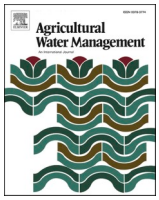

A fully remote sensing-based implementation of the two-source energy balance model: an application over Mediterranean crops

C. Cammalleri [a,*], M.C. Anderson [b], N.E. Bambach [c,d], A.J. McElrone [d,e], K. Knipper [c], M.C. Roby [c], G. Ciraolo [f], D. DeCaro [f], M. Ippolito [f], C. Corbari [a], A. Ceppi [a], M. Mancini [a], W.P. Kustas [b]

[a] Politecnico di Milano, Dipartimento di Ingegneria Civile e Ambientale (DICA), Milan, Italy
[b] Hydrology and Remote Sensing Lab, ARS, USDA, Beltsville, MD, USA
[c] Sustainable Agricultural Water Systems Research Unit, ARS, USDA, Davis, CA, USA
[d] Department of Viticulture and Enology, University of California, Davis, USA
[e] Crops Pathology and Genetics Research, ARS, USDA, Davis, CA, USA
[f] Università degli Studi di Palermo, Dipartimento di Ingegneria, Palermo, Italy

ARTICLE INFO

Keywords:
Cold and hot pixels
Landsat
TSEB
Evapotranspiration

ABSTRACT

Applications of the two-source energy balance (TSEB) scheme require either in-situ meteorological data to characterize the upper boundary conditions or the implementation of complex multi-scale approaches (ALEXI/DisALEXI). Over remote areas, detailed meteorological forcing (i.e., air temperature and wind speed) are often missing, limiting the quality of the simulated fluxes. To compute surface energy fluxes, the use of wet and dry boundary conditions, commonly referred to as hot and cold pixels, is a widely adopted strategy in thermal-based, single-source surface energy balance models for defining the relationship between satellite land-surface temperature (LST) and the surface-atmosphere temperature gradient. This contextual scaling approach reduces model sensitivity to biases in LST retrievals, but it has been previously tested within the TSEB modelling framework only in limited capacity. An automatic procedure for retrieving the two boundary temperatures is here proposed, removing the need for external meteorological data and leading to temperature values that are unbiased compared to ideal estimations (from in-situ observations) and characterized by deviations on the order of 1.5 and 4.5 °C for cold and hot conditions, respectively. Despite the lower accuracy in the hot pixel temperature, this does not seem to significantly affect the overall capability of the model to reproduce observed fluxes, with errors in instantaneous sensible and latent heat fluxes in the order of 60 W m^{-2} (slightly above 1 mm d^{-1} on daily evapotranspiration) over a set of 16 sites in the US and Italy, characterized by typical Mediterranean crops. The proposed TSEB implementation is fully remote sensing based, meaning satellite-consistent retrievals of air temperature and wind speed are obtained directly from information available within the satellite scene itself. This approach represents a suitable alternative to accurately model evapotranspiration and other surface energy fluxes in the absence of reliable meteorological data.

1. Introduction

The increasing availability of satellite remote sensing observations of land-surface temperature (LST) has fuelled the application of residual surface energy balance (SEB) models. These models partition available surface energy into latent and sensible heat fluxes, with a significant focus on mapping actual evapotranspiration (ET) over agricultural lands due to their ability to cover large areas with high spatial detail, ranging between 10 and 100 m - a feat unattainable with in-situ observations (Chan and Liu, 2020).

There is an extensive list of SEB modelling approaches in the literature (see McShane et al., 2017; García-Santos et al., 2022), with models generally categorized into single- or two- source approaches. The former solve the SEB for a combined soil and vegetated surface, while the latter treat these components separately. All SEB models, regardless of their classification, rely on auxiliary information about atmospheric

* Corresponding author.
E-mail address: carmelo.cammalleri@polimi.it (C. Cammalleri).

https://doi.org/10.1016/j.agwat.2024.109207
Received 4 July 2024; Received in revised form 31 October 2024; Accepted 28 November 2024

conditions on top of the land surface. Specifically, air temperature data are key in defining the surface-atmosphere temperature gradient, and wind speed is vital for modelling flux resistances.

Kustas and Norman (1996) identified a major challenge in using satellite-based LST in SEB applications: inconsistencies between air temperature and LST measurements (Anderson et al., 2024). To address this issue, satellite-based SEB models like the Surface Energy Balance Algorithm for Land (SEBAL, Bastiaanssen et al., 1998) and the Mapping Evapotranspiration at High Resolution with Internalized Calibration (METRIC, Allen et al., 2007) have introduced empirical linear relationships between LST and temperature gradient for modelling sensible heat (H). These models rely on defining two end-member conditions, a hot/dry pixel where the latent heat (λET) is minimal or zero and a cold/wet pixel where λET is at its potential, to accurately model heat fluxes (Allen et al., 2007).

The Simplified Surface Energy Balance (SSEB) approach, introduced by Senay et al. (2007), assumes a linear relationship between latent heat flux and the temperature gradient between hot and cold pixel conditions. Since early inception of these contextual scaling SEB approaches, major efforts have been dedicated to the automatic retrieval of the boundary conditions for operational applications (Allen et al., 2013).

In the context of the two-source modelling framework, potential inconsistencies between air temperature and LST have been addressed using either multi-temporal (Anderson et al., 1997; Anderson et al., 2007; Norman et al., 2000) or multi-scale (Anderson et al., 2004; Norman et al., 2003) methodologies. For satellite data acquired multiple times per day (e.g., geostationary satellites), the Atmosphere-Land Exchange Inverse (ALEXI, Anderson et al., 2007) and the Dual Temperature Difference (DTD, Norman et al., 2000) approaches exploit differences in LST over time to minimize inconsistencies with air temperature. As a downscaling approach for ALEXI, the DisALEXI method (Norman et al., 2003) uses air temperature estimations from ALEXI as upper boundary conditions for the SEB, with both ALEXI and DisALEXI based on the well-established two-source energy balance (TSEB) modelling scheme (Norman et al., 1995).

On the one hand, approaches like ALEXI and DTD are only suitable for geostationary satellite, and they cannot be applied to high resolution data, such as Landsat, currently available at best every 8 days. On the other hand, multi-scale applications like ALEXI/DisALEXI can be computationally intense, as they rely on the implementation of both models over a given region. Direct applications of TSEB using reanalysis data are also available in the literature. Guzinski et al. (2020) developed Sen-ET, an application of the TSEB algorithm using Sentinel data and meteorological data from ERA5 reanalysis. Similarly, Jaafar et al. (2022) implemented TSEB within the Google Earth Engine (GEE, Gorelick et al., 2017) platform using ERA5Land for meteorological forcing. However, it is well documented how reanalysis products may be characterized by significant biases over many regions (e.g., Choudhury et al., 2023; Zou et al., 2022); this, combined with possible inaccuracy in LST calibration, can lead to large errors in ET estimates.

In general, while the use of end member λET values associated with hot and cold pixels is quite extensive in single-source models, only a few applications of this approach in two-source formulations are available. The Enhanced Two-Source Evapotranspiration Model for Land (ETEML; Yang et al., 2015) incorporates a theoretically-defined trapezoidal LST-vegetation index, similar to the triangle method introduced by Price (1990) for ET and soil moisture retrieval (Carlson, 2007), in a two-source modelling scheme. A first attempt at incorporating boundary conditions into the TSEB modelling scheme is reported by Cammalleri et al. (2012), where TSEB was applied to airborne images using LST-consistent air temperatures derived from a water body within the scenes. A potential advantage of incorporating boundary conditions into the TSEB model is that it does not require an empirically derived LST-temperature gradient relationship to operate, unlike SEBAL and METRIC, hence allowing for the estimation of additional meteorological variables (e.g., wind speed). Previous studies have demonstrated how wind speed, albeit less important, still plays a role in ET modelling for defying aerodynamic resistances (Ambas and Baltas, 2012).

The main goal of this study is to assess the extent to which automatically-calibrated LST end members can be successfully derived from the data themselves, and how they can be incorporated within the TSEB modelling scheme. This integration introduces a novel, fully remote sensing-based TSEB model that does not rely on external sources for air temperature or wind speed data. The proposed approach is tested over a large set of sites equipped with eddy covariance installations in California, USA, and in Italy, with a special focus on typical Mediterranean tree crops.

2. Material and methods

In this section, the ground and satellite datasets used for the analyses are introduced, along with the fundamentals of TSEB modelling and the strategy proposed for automatically assessing boundary conditions.

2.1. In-situ datasets

The study sites encompass 13 locations in California (USA) and 3 sites in Italy (Table 1), all characterized by a typical Mediterranean climate featuring dry and hot summers during the growing season. The crop types at these sites are predominately tree crops, including olive, citrus, vineyard, almond, and walnut. Field sizes range from approximately 1 to 30 ha, exhibiting a variety of canopy coverage and understory crop conditions.

All the sites are equipped with eddy covariance instrumentations for the measurement of sensible (H) and latent (λET) heat fluxes, as well as flux plates and 4-component net radiometers for the measurement of the available energy (difference between net radiation, R_n, and soil heat flux, G_0). Data records for all main fluxes are generated at half-hourly time steps. Auxiliary instruments for the measurement of standard meteorological variables (air temperature, T_a, solar radiation, R_s, and wind speed, U) are also included. Energy balance closure exceeded 75 % for all data analysed, with observations for evaluating the modelled fluxes derived by enforcing closure using the Bowen-ratio method (Twine et al., 2000).

In-situ observations of radiometric surface temperature (T_{rad}) were derived from the measured incoming and outgoing longwave components as in Nieto et al. (2019), while roughness parameters are derived from tabled crop type-based (see Table 1) canopy height values.

Ground data in the vineyard sites listed in Table 1 were collected as part of the GRAPEX experiment (Kustas et al., 2018), whereas the olive and almond sites are part of the T-REX project (Bambach et al., 2024). Additional details on the Italian sites can be found in Ippolito et al. (2023) for CIA, Cammalleri et al. (2013) for CTV, and Corbari et al. (2023) for FOR (see Table 1 for the locations of these sites).

2.2. Satellite data

Landsat 8 and 9 data over the 16 study sites were collected using Google Earth Engine (Gorelick et al., 2017). Only scenes acquired during the typical growing season, from April to September, and with less than 70 % cloud coverage were used. Water bodies, clouds and cloud shadows were masked using the quality flag distributed with the dataset, and duplicate dates (multiple scenes on the same date due to overlap) were removed. After this screening, the number of scenes reported in Table 1 was obtained for each study site, with an average of almost 2.5 scenes/month before 2022 and 4.5 scenes/month after the launch of Landsat 9 in late 2021.

TSEB simulations were performed at field scale, hence field-average values of albedo, LST, and NDVI were derived for each scene from the Landsat standard products. Landsat LST data are obtained from the single-channel atmospheric compensation algorithm using observations for the Thermal InfraRed Sensor (TIRS) band 10 (United State

Table 1
Summary description of the study sites. Note that Landsat 9 data are available only for 2022 and 2023, doubling the acquisition frequency.

ID	Crop	Period	Lat	Lon	Elevation	# scenes
CIA (Italy)	Citrus	2019–2022	38.08	13.42	30	81
CTV (Italy)	Olive	2015–2016	37.64	12.85	120	25
FOR (Italy)	Walnut	2019–2021	44.18	12.04	40	40
BAR_A12	Vineyard	2019–2021	38.75	−122.97	104	28
BAR_A07	Vineyard	2019–2020	38.75	−122.98	111	17
FLT_001	Vineyard	2023	38.50	−122.77	36	33
SLC_001	Vineyard	2023	38.49	−122.83	21	33
RIP_720	Vineyard	2019–2021	36.85	−120.17	61	60
RIP_760	Vineyard	2019–2021	36.84	−120.21	57	60
WWF	Almonds	2021–2022	38.66	−121.89	37	32
VAC	Almonds	2021–2022	38.30	−121.91	17	32
OLA	Almonds	2021–2022	36.80	−120.21	57	53
ORO_022	Olives	2023	39.37	−121.57	36	20
ORO_043	Olives	2023	39.36	−121.47	32	20
COR_CS3	Olives	2023	39.88	−122.15	93	36
ART_011	Olives	2023	39.60	−122.25	57	36

Geological Survey (USGS) (USGS), 2021). The original spatial resolution of TIRS is about 100-m, which is coarser than the optical sensor resolution (30-m). All standard level-2 Landsat products are distributed on a 30-m resolution grid, with LST obtained by applying a cubic convolution resampling. Thermal sharpening of the raw Landsat data to 30-m resolution was performed using the Data Mining Sharpening (DMS) technique (Gao et al., 2012), which is based on building a cubist regression tree between LST and all seven Landsat optical bands. The DMS can be applied either locally or on a full scene; in this study, the method was applied locally over a 10×10 km^2 spatial window centred on each study site. This choice increases consistency with the procedure used for the selection of end members (see Section 2.4).

2.3. The TSEB model

The Two-Source Energy Balance (TSEB) model (Norman et al., 1995) solves the surface energy balance separately for soil and canopy components of a region by assuming that the observed area is a mixture of the two sources. Remotely sensed LST is related to canopy (T_c) and soil (T_s) surface temperature through the relationship:

$$LST = [f_c T_c + (1 - f_c) T_s]^{1/4}, \quad (1)$$

where f_c is the fraction cover at the sensor view angle (assumed to be nadir for Landsat data).

A key step of the TSEB model is the estimation of the available energy – the difference between net radiation (R_n) and soil heat flux (G_0) - and the partitioning of this quantity in sensible and latent heat fluxes. In the estimation of the available energy, solar radiation represents an essential meteorological input, and is assumed to be equal to the clear-sky radiation (R_{so}) at the time of a usable satellite overpass, which can be derived from satellite observations along with valid *LST* observations.

Sensible heat fluxes from the soil and canopy (H_s and H_c) directly depend on both surface (T_c and T_s) and air (T_a) temperatures, as well as on flux resistances (which depend on above-canopy wind speed, U). The model determines canopy transpiration (λET_c) and soil evaporation (λE_s) through an iterative procedure, starting from the hypothesis of potential transpiration based on the Priestley-Taylor formulation for the canopy component (requiring only T_a and R_{so} as inputs) and gradually reducing this flux until non-negative soil evaporation is observed during daytime (Agam et al., 2010). Latent heat flux ($\lambda ET = \lambda ET_c + \lambda E_s$) assessments at satellite overpass time are upscaled to daily timescale by preserving the ratio between latent heat and solar radiation (Cammalleri et al., 2014).

2.3.1. TSEB-local

When the TSEB model is applied using local meteorological observations derived from a weather station (TSEB-local from hereafter), the consistency between in-situ LST (T_{rad}, see previous Section 2.2) and observed T_a is ensured by a proper calibration of the local sensors used to monitoring all the key quantities. This assumption can be also extended to wind U, given that weather stations are often located either on the same location or in close proximity of the study site. In this study, observations derived from the eddy covariance stations (Section 2.2) are used as inputs for the TSEB-local application.

2.3.2. TSEB-ERA5Land

For remote sensing-based applications, and in absence of local weather stations, the TSEB model can be forced with satellite-observed LST (i.e., Landsat) combined with reanalysis products. An example of such application is the approach proposed by Jaafar et al. (2022), which used ERA5Land (Muñoz-Sabater et al., 2021) reanalysis data from the European Centre Medium-range Weather Forecast (ECMWF) to define the upper boundary conditions (hereafter TSEB-ERA5Land). ERA5Land provides global meteorological data at a spatial resolution of 10-km by performing a lapse-rate correction on temperature due to the different altitude in ERA5 and ERA5-Land grids (Dutra et al., 2020).

2.4. TSEB fully remote sensing-based implementation

The modification of the TSEB model proposed here does not alter the original formulation, used in both TSEB-local and TSEB-ERA5Land, in any meaningful way, but just replaces the T_a and U derived from either in-situ data or reanalysis with estimations derived from end members as described in the next sub-section.

2.4.1. Definition of end member conditions

Information within a satellite scene can be used to infer self-consistent boundary conditions, such as the hot and cold temperature end members used in SEBAL and METRIC, among other methods. The concept beyond the use of these end members is to define upper and lower limits on λET, which are defined here for each study site – following an automatic procedure – using the remote sensing observations in a 10×10 km^2 spatial window. Indeed, a difference between the procedure proposed here and the approach adopted in either SEBAL or METRIC is the search for suitable LST end members only in the surrounding of the site of interest, rather than over an entire Landsat scene. While the use of information from the full scene may increase the likelihood of finding ideal LST end members, the spatial variability of meteorological conditions over such a large area (about 180×180 km^2) and the likelihood of encompassing many different landcover types may limit the local reliability of these estimations, and, in particular, the assumption of spatial invariance in the LST-temperature gradient relationship. However, to overcome the potential limitations derived from the application on a reduced area, a mix of observed data and theoretical considerations are employed.

First, LST and NDVI (normalized difference vegetation index) are aggregated at 90-m resolution following a simple average and masked over non-agricultural lands. This spatial aggregation ensures to remove from the successive analyses spurious pixels with extreme conditions. The cultivated area classification as part of the USDA/NASS cropland data layers is used for the US (Li et al., 2024), while the agricultural area classes in the Corine land use is used for Italy (Copernicus Land Managements Service (CLMS) (CLMS), 2021). Secondly, homogeneous pixels at coarse spatial resolution are searched using the coefficient of variation (CV < 0.1). This procedure is analogous to the one adopted in the TsHARP algorithm for thermal data sharpening (Kustas et al., 2003). Third, a NDVI-LST linear regression on the homogenous pixels is performed to derive the parameter of the regression (m and b) as well as the average deviation around the regression line (sd). Finally, the two end member temperatures, T_{cold} and T_{hot}, are estimated as:

$$T_{cold} = b + (NDVI_{cold} m) - 1.25 sd, \quad (2)$$

$$T_{hot} = b + (NDVI_{hot} m) + 1.25 sd, \quad (3)$$

where $NDVI_{cold}$ and $NDVI_{hot}$ are the NDVI values corresponding to full coverage (0.8) and bare soil (0.2) conditions, respectively, and 1.25 (-1.25) is the standardized z-score corresponding to the 90-th (10-th) percentile in the case of standard normally distributed data. The obtained boundary conditions are visually represented in Fig. 1 for an example case study.

The use of Eqs. (2) and (3), rather than actual observed values of T_{cold} and T_{hot}, aims at ensuring that consistent estimates are obtained even if actual extreme conditions (i.e., of λET=0 and λET at the potential rate, or of NDVI = 0.8 and NDVI = 0.2) are not directly observed surrounding the study site.

2.4.2. Estimation of meteorological forcing from end members

The two boundary conditions are not used here to generate an empirical temperature-gradient linear relationship, but rather to define two key TSEB meteorological upper boundaries. These variables need to achieve the goals of: 1) minimizing the inconsistency with LST derived from satellite, and 2) removing the need for auxiliary meteorological information. With the two boundary temperatures derived as in Section 2.4.1, both air temperature and wind speed can be inferred.

Air temperature values used in the TSEB model are assumed equal to T_{cold} (i.e., H=0), while wind speed estimations (namely U_{hot}) are derived from T_{hot} under the assumption of a bare soil with null evaporation ($\lambda E_s = 0$). In particular, wind speed can be derived from the aerodynamic resistance above the dry soil, computed as:

$$R_{a,hot} = \frac{\rho C_p (T_{hot} - T_{cold})}{R_{n,hot} - G_{0,hot}}, \quad (4)$$

$$U_{hot} = \frac{\left[\ln\left(\frac{z_U}{z_{om}}\right) - \Psi_m\right]\left[\ln\left(\frac{z_T}{z_{oh}}\right) - \Psi_h\right]}{k^2 R_{a,hot}}, \quad (5)$$

where ρC_p is the air volumetric heat capacity, the air temperature is assumed equal to T_{cold}, the soil sensible heat is equal to the available energy ($H_{hot} = R_{n,hot} - G_{0,hot}$). z_{om} and z_{oh} are the roughness parameters for a bare soil, z_U and z_T are the measurement heights of wind and temperature over the surface (set equal to 10 and 2 m, respectively), and Ψ_m and Ψ_h are the stability correction functions (Webb, 1970). Given the particular conditions in which Eq. (5) is applied (high sensible heat and null evapotranspiration), the atmospheric condition is always expected to be unstable. This retrieval procedure assumes that air temperature and wind speed are constant over the 10 × 10 km^2 area associated with the hot and cold pixel selections. It is worth mentioning that a similar hypothesis of spatial homogeneity in meteorological forcings is also done for the TSEB-ERA5Land (given the resolution of ERA5Land data) or when the weather station is not directly located over the study field (for the TSEB-local).

To separate the effects of using end members only for the retrieval of air temperature (T_{cold}) or for the estimation of both air temperature and wind speed, the TSEB executed using only the cold pixel is referred to as TSEB-C hereafter, whereas the model version that incorporates both cold and hot pixels (i.e., fully remote sensing based) is instead referred to as TSEB-CH.

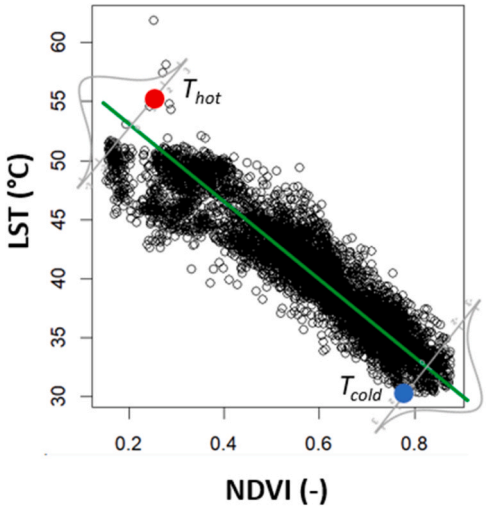

Fig. 1. Example of estimation of the boundary conditions. LST and NDVI data correspond to retrievals over the OLA site (see Table 1) for the date July 13th, 2021.

3. Results

3.1. TSEB-local and TSEB-ERA5Land applications

SEB models may be characterized by large uncertainty in some applications, so considerations on the accuracy of TSEB-C and TSEB-CH models may be affected by the capability of TSEB itself to reproduce the observed fluxes. For this reason, the general reliability of TSEB over the study sites was assessed, as a future benchmark, by preliminary running the TSEB-local on all the study sites. The results of this analysis are summarized in Fig. 2, where all the sites are pooled together in a single set of plots.

Overall, the TSEB model performs satisfactorily, with a mean absolute difference (MAD) slightly above 40 W m^{-2} for all the main components of the energy balance, namely $R_n - G_0$, H and λET, and a very limited negative bias (mean difference, MD, lower than 0). Some differences can be observed in the performance of the single sites, as summarized by the MAD value reported for each site in Table 2. Accuracy is generally higher for R_n and G_0 at all sites, with MAD values for turbulent fluxes reaching a maximum of 92 and 82 W m^{-2} for H in ORO_022 and λET in VAC, respectively.

As an additional benchmark, The TSEB model was also applied to actual Landsat LST data using ERA5Land atmospheric forcings (T_a and U) instead of tower observations. These simulations aim at evaluating the reliability of the model in absence of local consistent information. The results are summarized in Fig. 3 and Table 3 for all the data combined and the single sites, respectively.

TSEB estimations of the available energy do not seem particularly affected by the use of ERA5Land air temperature and Landsat LST instead of local data in these cases, with accuracy and bias comparable to TSEB-local (see Fig. 2a *vs.* Fig. 3a). On the contrary, accuracy in turbulent fluxes is reduced, with MAD values doubled compared to the local applications (e.g., MAD = 44 W m^{-2} in Fig. 2c for λET *vs.* 99 W m^{-2} in Fig. 3c). Overall, some of the differences seem to be caused

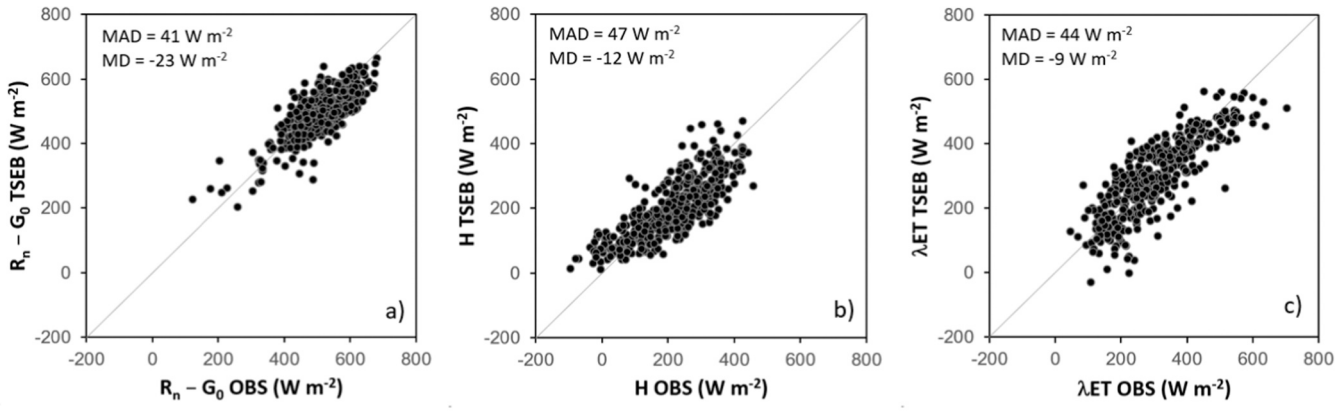

Fig. 2. Comparison between local application of the TSEB and observed fluxes at the Landsat overpass times for all 16 sites. Panel a) compares the available energy, panel b) the sensible, and panel c) the latent heat fluxes.

Table 2
Mean absolute difference (MAD) values computed separately for each flux and site between observations and TSEB-local.

Site	# data	R_n	G_0	H	λET
CIA	69	16	58	69	62
CTV	19	32	67	77	71
FOR	22	22	27	83	71
BAR_A07	17	45	36	41	40
BAR_A12	24	20	26	43	70
FLT_001	25	32	15	46	35
SLC_001	23	25	31	44	28
ORO_022	11	20	60	92	61
ORO_043	11	13	31	43	41
COR_CS3	26	24	43	42	50
ART_011	20	22	39	68	50
RIP_720	41	24	23	57	63
RIP_760	54	21	24	58	58
OLA	44	35	30	39	42
VAC	23	34	44	51	82
WWF	25	59	25	70	54

by an increased tendency to underestimate the observed H (negative MD values) and consequently overestimate the λET (MD = 32 W m^{-2}). However, an opposite behaviour is observed for the highest(lowest) H (λET) values, with a tendency for the model to overestimate(underestimate) the observations. Results obtained for each site show how MAD values are above 100 W m^{-2} in 9 out of 16 sites for λET (see Table 3), further stressing how inconsistencies in surface and atmospheric data seem to affect more strongly the residual term of the SEB.

3.2. Evaluation of the automatically detected boundary conditions

The procedure described in Section 2.4.1 was applied independently for each date and site to retrieve Landsat-based T_{cold} and T_{hot} estimates. To obtain a reference dataset for the evaluation of these satellite estimates, in-situ retrieval of T_{cold} and T_{hot} (namely '-ref' hereafter) are derived from T_a and U local observations. As one of the goals of using T_{cold} is to remove the effects of systematic differences between satellite

Table 3
Mean absolute difference (MAD) values computed separately for each flux and site between observations and TSEB-ERA5Land.

Site	# data	R_n	G_0	H	λET
CIA	69	36	55	134	195
CTV	19	31	55	97	146
FOR	22	23	31	119	124
BAR_A07	17	46	35	108	136
BAR_A12	24	24	26	117	139
FLT_001	25	39	16	91	102
SLC_001	23	24	30	102	86
ORO_022	11	22	60	94	89
ORO_043	11	17	32	66	54
COR_CS3	26	24	41	82	78
ART_011	20	24	37	87	91
RIP_720	41	29	23	64	95
RIP_760	54	29	25	93	121
OLA	44	57	30	74	109
VAC	23	30	44	47	71
WWF	25	77	26	99	138

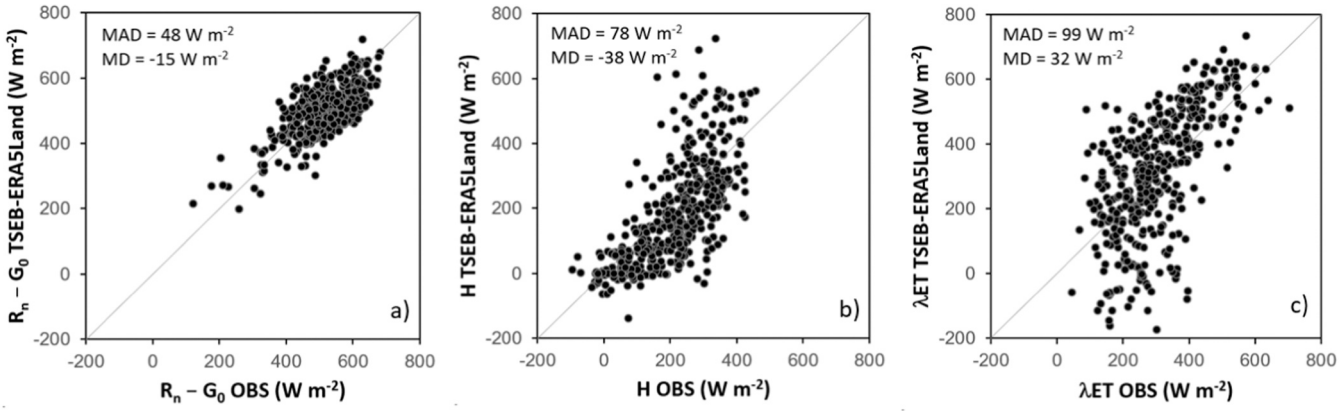

Fig. 3. Comparison between application of the TSEB using ERA5Land meteorological data and observed fluxes at the Landsat overpass times for all 16 sites. Panel a) compares the available energy, panel b) the sensible, and panel c) the latent heat fluxes.

and in-situ retrievals, $T_{cold\text{-}ref}$ is obtained by adding/subtracting the systematic bias in Landsat LST (LST – T_{rad}) to the observed air temperature, whereas $T_{hot\text{-}ref}$ is obtained by solving Eq. (4) for T_{hot} starting from observed U values.

The plots in Fig. 4 show the comparison between the Landsat derived and in-situ reference T_{cold} (panel a) and T_{hot} (panel b) values for all sites. In general, T_{cold} estimates are more accurate, with a limited bias (MD = 0.13 °C) and differences compared to the typical LST uncertainty. T_{hot} is characterized by a higher scatter, with a slightly larger bias (MD = 0.44 °C) and a MAD more than double the value for T_{cold}.

Since T_{hot} estimates can be seen as an alternative way to express U as a temperature (via Eq. 4), U values from ERA5Land can also be converted to equivalent T_{hot}, in order to obtain a dataset directly comparable with Landsat estimates. The results in Fig. 5 report T_{cold} (equal to the ERA5Land T_a) and T_{hot} estimations based on ERA5Land, highlighting how overall higher differences and biases are observed for both quantities compared to Landsat. The most remarkable differences can be observed in the overall accuracy of T_{cold} (MAD = 1.43 °C for Landsat *vs.* 2.29 °C for ERA5Land) and the bias in T_{hot} (MD = 0.44 °C for Landsat *vs.* 3.29 °C for ERA5Land).

Results for T_{hot} are also analysed in term of wind speed, as U represents the original variable assessed via Eq. (5). The data in Fig. 6 show the comparison between observed and Landsat modelled values (panel a), highlighting a good consistency for the large bulk of data at the centre of the scatterplot, but also the presence of some outliers, especially for high wind speed values (> 3 m s^{-1}). The results in Fig. 6b show the analogous comparison for ERA5Land, highlighting also in this case a considerable scatter. Overall, the better consistency of Landsat estimates compared to ERA5Land in terms of T_{hot} (see Fig. 4b *vs.* 5b) seems driven by the reduced bias in wind speed (MD = −0.12 and −0.58 m s^{-1}, respectively).

3.3. Application of TSEB-C and TSEB-CH

Based on the results reported in Section 3.2, and the difference in accuracy for T_{cold} and T_{hot} Landsat estimates, two separate applications of the revised TSEB model were performed. In the first, both T_{cold} and T_{hot} were used to replace in-situ observed T_a and U. In the second, T_{cold} only is used, while in-situ observed wind speed was still used.

The plots in Fig. 7 report the results for the fully remote sensing-based application, in which both T_{cold} and T_{hot} were used (namely TSEB-CH). As it can be observed, the model performs slightly worse than the TSEB-local, with MAD in the turbulent fluxes of about 60 W m^{-2} (an increase of about 15 W m^{-2} compared to the results reported in Fig. 3). However, the accuracy of TSEB-CH is considerably higher than that of TSEB-ERA5Land (Fig. 3). This is especially true for λET, with a reduced MAD (68 W m^{-2} vs. 99 W m^{-2}) and virtually no systematic bias.

Given the different accuracy observed for T_{cold} and T_{hot}, it is worth investigating which fraction of the reduction in accuracy is caused by each component. With this goal, the plots in Fig. 8 show the analogous results obtained using T_{cold} only (referred to as TSEB-C) for all the sites combined. Despite the high scatter observed in T_{hot} (see Fig. 4b), flux estimates are nearly identical to those in Fig. 8, with only a slight reduction in the average MAD for λET (from 68 to 63 W m^{-2}).

Since the performance for the two versions of the model is rather similar, subsequent analyses and discussions are focused on the TSEB-CH only. To complement the data in Fig. 7, Table 4 lists the MAD values for each individual site for TSEB-CH. It is worth highlighting how results for the TSEB-CH are better than TSEB-C (of at least 10 W m^{-2}) in few instances (marked in bold in Table 4), whereas the opposite (underlined values in Table 4) is a rarer occurrence.

Since many previous applications of the TSEB model focus on the modelling of daily ET, the results of different versions for this quantity are summarized in the boxplot in Fig. 9. In this case, instantaneous ET at the satellite overpass time is upscaled to daily ET by conserving the ratio of latent heat to solar radiation, as suggested by Cammalleri et al. (2014). It is worth mentioning how daily solar radiation data are required in this step. While local observations of daily solar radiation are used here for all TSEB model versions, reliable satellite estimates can be obtained using data from geostationary satellites (e.g., Blanc et al., 2011; Gracia Amillo et al., 2014), hence this step does not represent a practical limitation for remote sensing-based applications. These results show MAD values, on average, slightly above 1 mm d^{-1} for TSEB-CH, which compares to about 0.8 mm d^{-1} for TSEB-local and about 1.3 mm d^{-1} for TSEB-ERA5Land.

4. Discussion

The TSEB model has been validated as an effective method for estimating energy fluxes over agricultural lands in numerous studies (e.g., Anderson et al., 2005; Burchard-Levine et al., 2022; Cammalleri et al., 2010; Volk et al., 2024; Yang et al., 2017). Results presented here for the locally applied TSEB align with those studies, confirming that with accurate input data from local observations, the TSEB model achieves satisfactory accuracy (around 40–50 W m^{-2}, or a relative difference of 20–25 %). This level of accuracy is notably robust, particularly when considering that the typical accuracy of eddy covariance observations — under ideal conditions — is estimated to be about 10–15 % (Allen et al., 2011).

Outcomes of the TSEB-local model can be used as a benchmark, representing what is obtainable with the model under ideal conditions, including accurate local forcing for both LST and meteorological data. It is expected that satellite applications of the model will see a degradation in model performance, and this is well demonstrated by the results

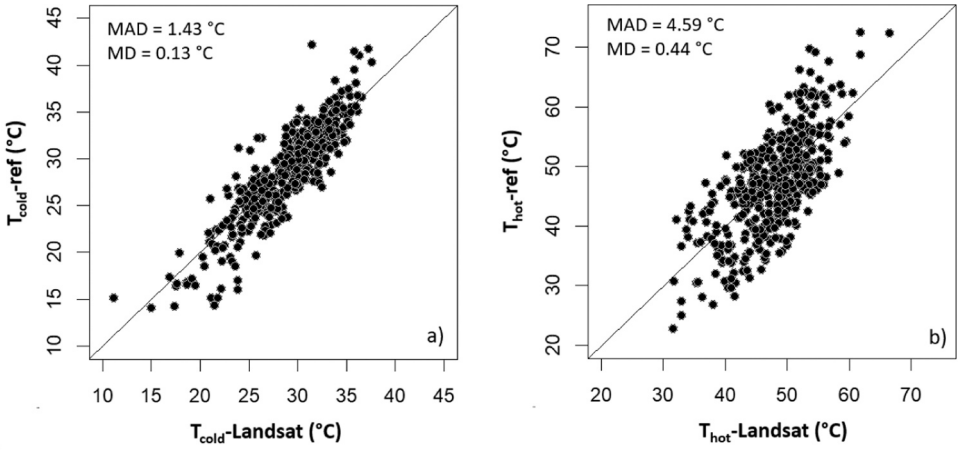

Fig. 4. Comparison between Landsat derived (x-axis) and in-situ reference (y-axis) cold (panel a) and hot (panel b) temperatures.

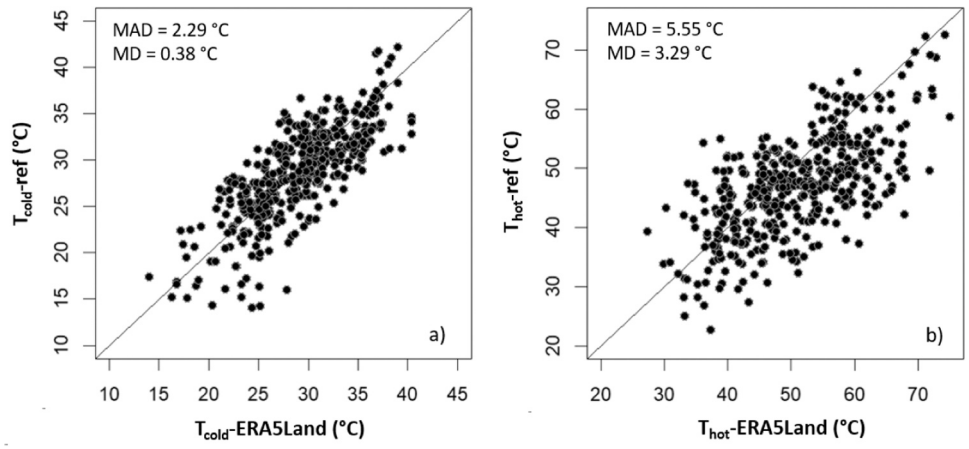

Fig. 5. Comparison between ERA5Land derived (x-axis) and in-situ reference (y-axis) cold (panel a) and hot (panel b) temperatures.

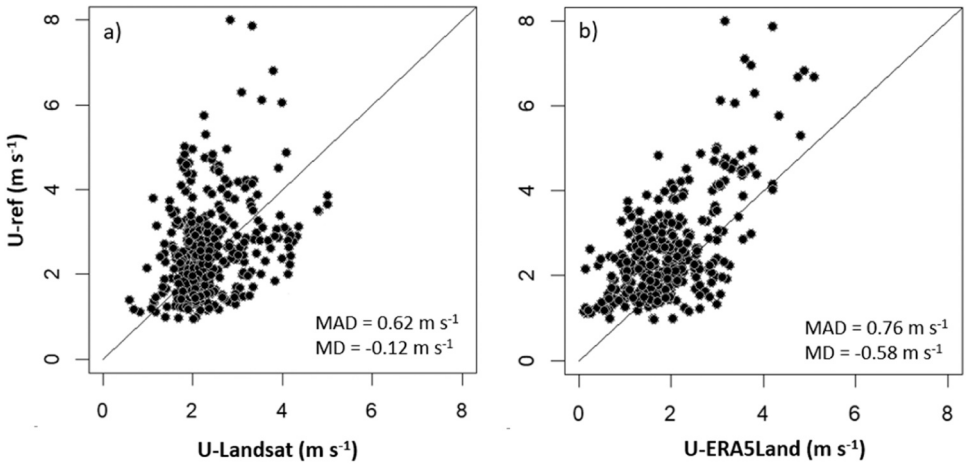

Fig. 6. Comparison between in-situ measured wind speed (ref, y-axis) and modelled data from Landsat hot pixel (panel a) and ERA5Land (panel b).

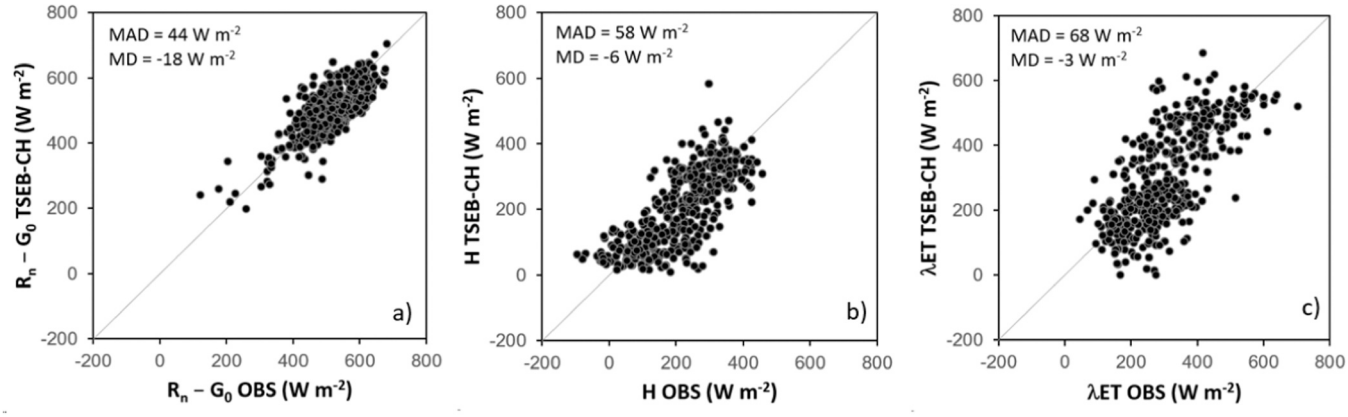

Fig. 7. Comparison between application of the TSEB using both Landsat T_{cold} and T_{hot} data (TSEB-CH) and observed fluxes for all 16 sites. Panel a) compares the available energy, panel b) the sensible, and panel c) the latent heat fluxes.

obtained using Landsat LST in conjunction to ERA5Land meteorological forcings. The reduction in accuracy, with errors that are more than double in the case of λET, can be ascribed not only to the reduced accuracy of reanalysis coarse-resolution (about 10-km) data compared to local in-situ observations, but most importantly to inconsistencies between surface and atmospheric datasets. This is demonstrated by the statistics for T_{cold} (Fig. 5a), which shows not only an increase in the systemic bias but also a greater scatter compared to the satellite estimates (Fig. 4a). As a consequence, a clear reduction in the accuracy of daily ET is also observed, with MAD reaching values above 1 mm d^{-1}. In this context, the results for the TSEB-ERA5Land support the conclusion that straightforward applications of TSEB over large areas may be characterized, in some cases, by limited accuracy, and that correction procedures implemented in approaches such ALEXI/DisALEXI are

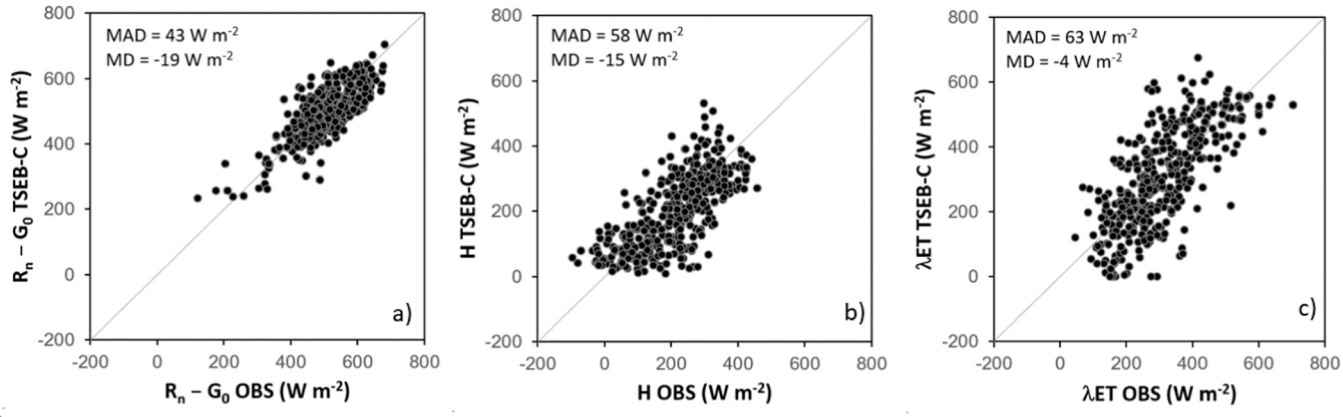

Fig. 8. Comparison between application of the TSEB using Landsat T_{cold} data (TSEB-C) and observed fluxes for all 16 sites. Panel a) compares the available energy, panel b) the sensible, and panel c) the latent heat fluxes.

Table 4
Mean absolute difference (MAD) values computed separately for each flux and site between observations and TSEB-CH. Values in bold (underlined) are at least 10 W m^{-2} lower (higher) for TSEB-CH compared to TSEB-C.

Site	# data	R_n	G_0	H	λET
CIA	69	15	63	57	107
CTV	19	48	72	98	97
FOR	22	34	32	68	96
BAR_A07	17	38	35	88	101
BAR_A12	24	21	25	**41**	**63**
FLT_001	25	37	15	57	66
SLC_001	23	18	32	59	36
ORO_022	11	17	58	**52**	**67**
ORO_043	11	16	31	50	**35**
COR_CS3	26	23	42	76	84
ART_011	20	24	37	70	72
RIP_720	41	22	23	70	80
RIP_760	54	18	25	74	82
OLA	44	45	27	60	61
VAC	23	38	44	77	98
WWF	25	84	26	**91**	149

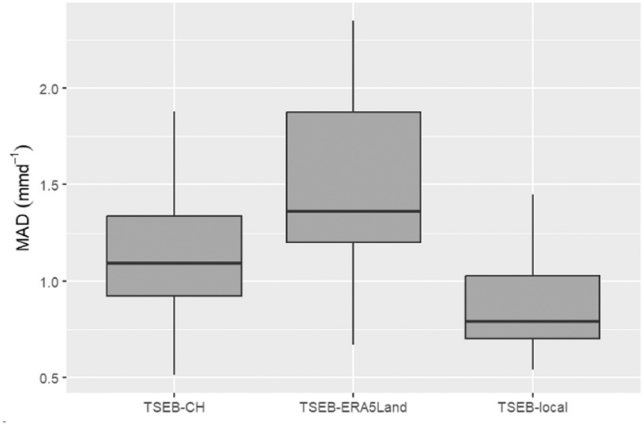

Fig. 9. Boxplot representing the distribution of the mean absolute difference (MAD) values between observed and modelled daily ET for the different versions of the TSEB model.

indeed key for accurate surface flux assessments. Some previous applications of TSEB using improved fusion of satellite inputs and reanalysis meteorological forcing have shown promising results in other regions over longer aggregation periods (10 days to month) (Guzinski et al., 2023), suggesting how the accuracy of the results may be related to the local accuracy of reanalysis products. It is worth highlighting how the results in this study are obtained during the growing season (April--September) only, when fluxes (and consequently errors) tend to be higher. Accuracy at annual scale or including winter season estimates may have lower errors on average.

As highlighted in Cammalleri et al. (2012), only a single additional boundary condition is needed in TSEB to remove inconsistencies in temperature data (to estimate an LST-consistent T_a), rather than determining two end member conditions as in single-source models (to calibrate the LST-gradient relationship). If we focus on T_{cold} only, the accuracy of the Landsat-consistent estimates obtained with the proposed procedure is quite high (MAD = 1.43 °C), with error comparable with the general uncertainty in LST products. As a reference, the automatic procedure for the selection of LST end members introduced by Allen et al. (2013) returned difference in the range 0.4–0.8 °C between automatic and manually selected cold pixels. The authors considered the effects of these differences negligible on ET estimates. In the same study, larger differences (about 2.2 °C) where observed for the hot pixel. Similarly, Saboori et al. (2021) reported larger uncertainty in defining T_{hot} compared to T_{cold}, while Morton et al. (2013) observed how the tail of the distribution in the hot end tends to have more variation than the cold tail. In addition, larger differences are expected for the hot pixel compared to the cold due to the higher magnitude of the temperature itself, as well as the wider divergence from air temperature; on the other hand, the larger scatter observed in our results may be ascribed to the attempt to relate T_{hot} to wind speed, which is highly variable across a landscape. The direct comparison of wind speed estimations with observed data further supports this assumption, as these relationships are characterized by large scatter, especially for high wind speed values (> 3 m s^{-1}). While Allen et al. (2013) observed that an error of about 2 °C in T_{hot} results in average error in H of around 35 W m^{-2} for METRIC, a lower sensitivity is observed here. This is likely because T_{hot} does not directly affect the computation of the temperature gradient in our methodology, as the gradient is modelled within the physics of the model using only T_{cold}. This feature of TSEB-CH is an advantage over other methods such as SEBAL and METRIC, as Long et al. (2011) observed a great sensitivity of SEBAL H estimates from both hot pixels LST and available energy.

Overall, the proposed method seems to return reliable estimations of the LST end members even by limiting the search to a domain on the order of 10 × 10 km^2 encompassing the site of interest. While this seems to be the case for all the analysed case studies, it can be an issue for very homogeneous regions, non-irrigated agricultural regions, or images acquired outside the growing seasons. In these circumstances, larger search areas may be preferable, and the variability in NDVI and LST data itself can be used to assess the suitability of the searched area. It is worth mentioning how even if the detection of cold and hot pixels is commonly

performed over the entire Landsat scene for both SEBAL and METRIC (e.g., Tasumi, 2019; Timmermans et al., 2007), Allen et al. (2013) indeed recommends locating the boundary conditions within 20–30 km of the location of the weather station to minimize inconsistencies. Morton et al. (2013) observed how high NDVI values (> 0.8) may be difficult to find in some circumstances; hence, our proposed approach to extract the boundary conditions from the regression line seems a good alternative to avoid relying directly on observed values.

The reduced accuracy of T_{hot} (and wind speed) compared to T_{cold} does not seem detrimental for the retrieval of the energy fluxes, on average, as supported by the results in Figs. 7 and 8, where no notable differences can be observed. Some studies have demonstrated how ET estimations can overcome the need of wind speed information (e.g., Mallick et al., 2018), hence the low sensitivity observed in this study to detailed retrieval of this variable is in agreement with these findings. In a few cases, MAD values are lower for TSEB-CH than for TSEB-C, suggesting that consistency may be preferred relative to overall accuracy. The accuracy of TSEB-CH on daily ET is, on average, only slightly above 1 mm d^{-1}, a value often observed in similar applications based on satellite data (e.g., Jaafar et al., 2022; Knipper et al., 2023).

From these results, it follows that the TSEB-CH methodology can be used to estimate surface energy fluxes without the need of auxiliary ground meteorological data. This allows for a direct application of the TSEB modelling scheme on Landsat (or similar) satellite data, without the need to retrieve additional information layers from ground sources. It is worth noting that daily solar radiation from satellite data are still needed for the instantaneous-to-daily upscaling, but this requirement does not represent a major drawback for satellite-based application given the increasing availability and reliability of solar radiation satellite retrievals. The application of this model version can be particularly useful in data scarce areas, or regions of the world where the accuracy of gridded meteorological forcing can be questionable. An additional application of this procedure can be in combination with the more sophisticated ALEXI/DisALEXI procedure, in which the upper boundary temperature condition for the high-resolution TSEB is derived from the coarse resolution (about 5-km) ALEXI simulations. In this case, T_{cold} estimates can be used as complementary information for cross-validation and uncertainty estimation of DisALEXI outputs. Overall, satellite-based ET estimates are still characterised by a less-than-ideal uncertainty in many applications (Pan et al., 2020); hence, the availability of multiple tools for the assessment of ET starting from similar modelling framework can be seen as a way to single out sources of error.

5. Summary and conclusions

The possibility to integrate additional boundary conditions defining LST end members (or hot and cold pixels) within the TSEB modelling scheme, similarly to models such as SEBAL and METRIC, was tested over a set of 16 sites in US and Italy characterized by tree crops in a typical Mediterranean climate, with the goal to introduce a fully remote sensing-based model that does not rely on any ground-based auxiliary information and that can reliably be applied also over data scarce regions.

In comparing the outcomes of this model (namely TSEB-CH) against a local implementation of TSEB (fully based on in-situ observations), it was possible to observe a general reduction in the overall performance, albeit with errors (MAD of about 60 W m^{-2}) that are still within the range of accuracy of most satellite-based applications. The detection of the so-called cold temperature (used as a proxy variable of the above-canopy air temperature) seems to be characterized by a higher accuracy (MAD of about 1.5 °C) compared to the hot temperature (used to estimate the above canopy wind speed). However, the lower accuracy in T_{hot} (and wind speed) does not seem detrimental for the overall capability of the model to reproduce observed sensible and latent fluxes. A clear improvement in the use of this methodology over a TSEB forced with ERA5Land reanalysis data was observed, stressing on the value of using consistent land-surface and atmospheric temperatures.

Possible applications of the proposed methodology are either stand-alone implementations of TSEB that will be completely independent from the need for accurate local auxiliary data, or the use as a complementary method to the more sophisticated ALEXI/DisALEXI approach for the assessment of the uncertainty in the retrieval of upper boundary temperature conditions. While quite extensive, the set of test sites used in this study still covers a relatively limited range of conditions, so further analyses are advisable over more homogeneous regions or non-irrigated areas, where the detection of proper boundary conditions within the limited searching window (10×10 km^2) may be more problematic.

CRediT authorship contribution statement

D. DeCaro: Writing – review & editing, Data curation. **M. Ippolito:** Writing – review & editing, Data curation. **C. Corbari:** Writing – review & editing, Data curation. **A. Ceppi:** Writing – review & editing, Data curation. **M. Mancini:** Writing – review & editing, Funding acquisition. **Carmelo Cammalleri:** Writing – review & editing, Writing – original draft, Methodology, Funding acquisition, Formal analysis, Conceptualization. **W.P. Kustas:** Writing – review & editing, Supervision, Methodology, Conceptualization. **M.C. Anderson:** Writing – review & editing, Supervision, Conceptualization. **N.E. Bambach:** Writing – review & editing, Data curation. **A.J. McElrone:** Writing – review & editing, Supervision, Data curation. **K. Knipper:** Writing – review & editing, Visualization, Methodology, Data curation. **M.C. Roby:** Writing – review & editing, Data curation. **G. Ciraolo:** Writing – review & editing, Data curation.

Declaration of Competing Interest

The authors declare that they have no known competing financial interests or personal relationships that could have appeared to influence the work reported in this paper.

Acknowledgements

Carmelo Cammalleri gratefully acknowledges financial support for this research by the Fulbright U.S. Student Program, which is sponsored by the U.S. Department of State and the U.S.-Italy Fulbright Commission. Its contents are solely the responsibility of the author and do not necessarily represent the official views of the Fulbright Program, the Government of the United States, or the U.S.-Italy Fulbright Commission. This research was partially founded by "Programma di ricerca, CN_00000022 "National Research Centre for Agricultural Tecnologies (Agritech)" finanziato dal Decreto Direttoriale di concessione del finanziamento n. 1032 del 17.06.2022 a valere sulle risorse del PNRR MUR – M4C2 – Investimento 1.4 - Avviso "Centri Nazionali" - D.D. n. 3138 del 16/12/2021 - Spoke 3 Enabling Technologies and sustainable strategies for the smart management of agricultural system and their environmental impact". The experimental installations are supported by the Almond Board of California (WATER16), California Department of Food and Agriculture Specialty Crop Grant Program (20–0001–031-SF), and American Vineyard Foundation (Project A23–3873). USDA is an equal opportunity provider and employer.

Data availability

Data will be made available on request.

References

Agam, N., Kustas, W.P., Anderson, M.C., Norman, J.M., Colaizzi, P.D., Prueger, J.H., 2010. Application of the Priestley-Taylor approach in a two-source surface energy balance model. J. Hydrometeorol. 11, 185–198. https://doi.org/10.1175/2009JHM1124.1.

Allen, R.G., Tasumi, M., Trezza, R., 2007. Satellite based energy balance for Mapping Evapotranspiration with Internalized Calibration (METRIC)—Model. J. Irr. Drain. Eng. 133 (4), 380–394. https://doi.org/10.1061/(ASCE)0733-9437(2007)133:4(380).

Allen, R.G., Pereira, L.S., Howell, T.A., Jensen, M.E., 2011. Evapotranspiration information reporting: I. Factors governing measurement accuracy. Agric. Water Manag. 98, 899–920. https://doi.org/10.1016/j.agwat.2010.12.015.

Allen, R.G., Burnett, B., Kramber, W., Huntington, J., Kjaersgaard, J., Kilic, A., Kelly, C., Trezza, R., 2013. Automated calibration of the METRIC-Landsat Evapotranspiration Process. J. Am. Water Resour. Ass. 49 (3), 563–576. https://doi.org/10.1111/jawr.12056.

Ambas, V.Th, Baltas, E., 2012. Sensitivity analysis of different evapotranspiration methods using a new sensitivity coefficient. Glob. NEST J. 14 (3), 335–343. https://doi.org/10.30955/gnj.000882.

Anderson, M.C., Norman, J.M., Diak, G.R., Kustas, W.P., Mecikalski, J.R., 1997. A two-source time-integrated model for estimating surface fluxes using thermal infrared remote sensing. Remote Sens. Environ. 60 (2), 195–216. https://doi.org/10.1016/S0034-4257(96)00215-5.

Anderson, M.C., Norman, J.M., Mecikalski, J.R., Torn, R.D., Kustas, W.P., Basara, J.B., 2004. A multiscale remote sensing model for disaggregating regional fluxes to micrometeorological scales. J. Hydrometeorol. 5 (2), 343–363. https://doi.org/10.1175/1525-7541(2004)005< 0343:AMRSMF> 2.0.CO;2.

Anderson, M.C., Norman, J.M., Kustas, W.P., Li, F., Prueger, J.H., Mecikalski, J.R., 2005. Effects of vegetation clumping on two–source model estimates of surface energy fluxes from an agricultural landscape during SMACEX. J. Hydrometeorol. 6 (6), 892–909. https://doi.org/10.1175/JHM465.1.

Anderson, M.C., Norman, J.M., Mecikalski, J.R., Otkin, J.A., Kustas, W.P., 2007. A climatological study of evapotranspiration and moisture stress across the continental United States based on thermal remote sensing: 1. Model formulation. J. Geophys. Res. 112 (D10), D10117. https://doi.org/10.1029/2006JD007506.

Anderson, M.C., Kustas, W.P., Norman, J.M., Diak, G., Hain, C., Gao, F., Yang, Y., Knipper, K., Xue, J., Yang, Y., Crow, W., Holmes, T., Nieto, H., Guzinski, R., Otkin, J., Mecikalski, J., Cammalleri, C., Torres-Rua, A., Zhan, X., Fang, L., Colaizzi, P., Agam, N., 2024. A brief history of the thermal IR-based Two-Source Energy Balance (TSEB) model – diagnosing evapotranspiration from plant to global scales. Agr. For. Meteorol. 350, 109951. https://doi.org/10.1016/j.agrformet.2024.109951.

Bambach, N., Knipper, K., McElrone, A., Nocco, M., Torres-Rua, A., Kustas, W., Anderson, M., Castro, S., Edwards, E., Duran-Gomez, M., Gal, A., Tolentino, P., Wright, I., Roby, M., Gao, F., Alfieri, J., Prueger, J., Hipps, L., Saa, S., 2024. The Tree-Crop Remote Sensing of Evapotranspiration Experiment (T-REX): A science-based path for sustainable water management and climate resilience. Bull. Am. Meteorol. Soc. 105 (1), E257–E284. https://doi.org/10.1175/BAMS-D-22-0118.1.

Bastiaanssen, W.G.M., Menenti, M., Feddes, R.A., Holtslag, A.A.M., 1998. A remote sensing surface energy balance algorithm for land (SEBAL) - 1. Formulation. J. Hydrol. 212–213, 198–212. https://doi.org/10.1016/S0022-1694(98)00253-4.

Blanc, P., Gschwind, B., Lefèvre, M., Wald, L., 2011. The HelioClim project: Surface solar irradiance data for climate applications. Remote Sens 3, 343–361. https://doi.org/10.3390/rs3020343.

Burchard-Levine, V., Nieto, H., Kustas, W.P., Gao, F., Alfieri, J.G., Prueger, J.H., Hipps, L. E., Bambach-Ortiz, N., McElrone, A.J., Castro, S.J., Alsina, M.M., McKee, L.G., Zahn, E., Bou-Zeid, E., Dokoozlian, N., 2022. Application of a remote-sensing three-source energy balance model to improve evapotranspiration partitioning in vineyards. Irr. Sci. 40, 593–608. https://doi.org/10.1007/s00271-022-00787-x.

Cammalleri, C., Anderson, M.C., Ciraolo, G., D'Urso, G., Kustas, W.P., La Loggia, G., Minacapilli, M., 2010. The impact of in-canopy wind profile formulations on heat flux estimation in an open orchard using the remote sensing-based two-source model. Hydrol. Earth Syst. Sci. 14, 2643–2659. https://doi.org/10.5194/hess-14-2643-2010.

Cammalleri, C., Anderson, M.C., Ciraolo, G., D'Urso, G., Kustas, W.P., La Loggia, G., Minacapilli, M., 2012. Applications of a remote sensing-based two-source energy balance algorithm for mapping surface fluxes without in situ air temperature observations. Remote Sens. Environ. 124, 502–515. https://doi.org/10.1016/j.rse.2012.06.009.

Cammalleri, C., Rallo, G., Agnese, C., Ciraolo, G., Minacapilli, M., Provenzano, G., 2013. Combined use of eddy covariance and sap flow techniques for partition of ET fluxes and water stress assessment in an irrigated olive orchard. Agric. Water Manag. 120, 89–97. https://doi.org/10.1016/j.agwat.2012.10.003.

Cammalleri, C., Anderson, M.C., Kustas, W.P., 2014. Upscaling of evapotranspiration fluxes from instantaneous to daytime scales for thermal remote sensing applications. Hydrol. Earth Syst. Sci. 18, 1885–1894. https://doi.org/10.5194/hess-18-1885-2014.

Carlson, T., 2007. An overview of the "Triangle Method" for estimating surface evapotranspiration and soil moisture from satellite imagery. Sensors 7 (8), 1612–1629. https://doi.org/10.3390/s7081612.

Chan, J.M., Liu, J., 2020. Evolution of evapotranspiration models using thermal and shortwave remote sensing data. Remote Sens. Environ. 237, 111594. https://doi.org/10.1016/j.rse.2019.111594.

Choudhury, D., Ji, F., Nishant, N., Di Virgilio, G., 2023. Evaluation of ERA5-simulated temperature and its extremes for Australia. Atmos 14 (6), 913. https://doi.org/10.3390/atmos14060913.

Copernicus Land Managements Service (CLMS), 2021. CORINE land Cover – Unser Manual version 1.0. 129 pp. Available at: ⟨https://land.copernicus.eu/en/products/corine-land-cover/clc2018⟩. [last access: March 2024].

Corbari, C., Paciolla, N., Rossi, G., Mancini, M., 2023. A double two-sources energy-water balance model for improving evapotranspiration estimates and irrigation management in fruit trees fields. Agric. Water Manag. 289, 108522. https://doi.org/10.1016/j.agwat.2023.108522.

Dutra, E., Muñoz-Sabater, J., Boussetta, S., Komori, T., Hirahara, S., Balsamo, G., 2020. Environmental lapse rate for high-resolution land surface downscaling: An application to ERA5. Earth Space Sci. 7, e2019EA000984. https://doi.org/10.1029/2019EA000984.

Gao, F., Kustas, W.P., Anderson, M.C., 2012. A data mining approach for sharpening thermal satellite imagery over land. Remote Sens 4 (11), 3287–3319. https://doi.org/10.3390/rs4113287.

García-Santos, V., Sánchez, J.M., Cuxart, J., 2022. Evapotranspiration acquired with remote sensing thermal-based algorithms: A state-of-the-art review. Remote Sens 14 (14), 3440. https://doi.org/10.3390/rs14143440.

Gorelick, N., Hancher, M., Dixon, M., Ilyushchenko, S., Thau, D., Moore, R., 2017. Google Earth Engine: Planetary-scale geospatial analysis for everyone. Remote Sens. Environ. 202, 18–27. https://doi.org/10.1016/j.rse.2017.06.031.

Gracia Amillo, A., Huld, T., Mueller, R.A., 2014. New database of global and direct solar radiation using the eastern Meteosat satellite, models and validation. Remote Sens 6 (9), 8165–8189. https://doi.org/10.3390/rs6098165.

Guzinski, R., Nieto, H., Sandholt, I., Karamitilios, G., 2020. Modelling high-resolution actual evapotranspiration through Sentinel-2 and Sentinel-3 data fusion. Remote Sens 12 (9), 1433. https://doi.org/10.3390/rs12091433.

Guzinski, R., Nieto, H., Rubén Ramo Sánchez, R.R., Sánchez, J.M., Jomaa, I., Zitouna-Chebbi, R., Roupsard, O., López-Urrea, R., 2023. Improving field-scale crop actual evapotranspiration monitoring with Sentinel-3, Sentinel-2, and Landsat data fusion. Int. J. Appl. Earth Obs. Geoinf. 125, 103587. https://doi.org/10.1016/j.jag.2023.103587.

Ippolito, M., De Caro, D., Ciraolo, G., Minacapilli, M., Provenzano, G., 2023. Estimating crop coefficients and actual evapotranspiration in citrus orchards with sporadic cover weeds based on ground and remote sensing data. Irr. Sci. 41, 5–22. https://doi.org/10.1007/s00271-022-00829-4.

Jaafar, H.H., Mourad, R.M., Kustas, W.P., Anderson, M.C., 2022. A global implementation of single- and dual-source surface energy balance models for estimating actual evapotranspiration at 30-m resolution using Google earth engine. Water Resour. Res. 58 (11), e2022WR032800. https://doi.org/10.1029/2022WR032800.

Knipper, K., Anderson, M., Bambach, N., Kustas, W., Gao, F., Zahn, E., Hain, C., McElrone, A., Belfiore, O.R., Castro, S., Alsina, M.M., Saa, S., 2023. Evaluation of partitioned evaporation and transpiration estimates within the DisALEXI modeling framework over irrigated crops in California. Remote Sens 15, 68. https://doi.org/10.3390/rs15010068.

Kustas, W.P., Norman, J.M., 1996. Use of remote sensing for evapotranspiration monitoring over land surfaces. Hydrol. Sci. J. 41, 495–516. https://doi.org/10.1080/02626669609491522.

Kustas, W.P., Norman, J.M., Anderson, M.C., French, A.N., 2003. Estimating subpixel surface temperatures and energy fluxes from the vegetation index-radiometric temperature relationship. Remote Sens. Environ. 85, 429–440. https://doi.org/10.1016/S0034-4257(03)00036-1.

Kustas, W.P., Anderson, M.C., Alfieri, J.G., Knipper, K., Torres-Rua, A., Parry, C.K., Nieto, H., Agam, N., White, W.A., Gao, F., McKee, L., Prueger, J.H., Hipps, L.E., Los, S., Alsina, M.M., Sanchez, L., Sams, B., Dokoozlian, N., McKee, M., Jones, S., Yang, Y., Wilson, T.G., Lei, F., McElrone, A., Heitman, J.L., Howard, A.M., Post, K., Melton, F., Hain, C., 2018. The Grape Remote Sensing Atmospheric Profile and Evapotranspiration Experiment. Bull. Am. Meteorol. Soc. 99 (9), 1791–1812. https://doi.org/10.1175/BAMS-D-16-0244.1.

Li, H., Di, L., Zhang, C., Lin, L., Guo, L., Yu, E.G., Yang, Z., 2024. Automated in-season crop-type data layer mapping without ground truth for the Conterminous United States based on multisource satellite imagery. IEEE Trans. Geosc. Remote Sens. 62, 1–14. https://doi.org/10.1109/TGRS.2024.3361895.

Long, D., Singh, V.P., Li, Z.-L., 2011. How sensitive is SEBAL to changes in input variables, domain size and satellite sensor? Clim. Dynam 116, D21107. https://doi.org/10.1029/2011JD016542.

Mallick, K., Toivonen, E., Trebs, I., Boegh, E., Cleverly, J., Eamus, D., Koivusalo, H., Drewry, D., Arndt, S.K., Griebel, A., Beringer, J., Garcia, M., 2018. Bridging thermal infrared sensing and physically-based evapotranspiration modeling: From theoretical implementation to validation across an aridity gradient in Australian ecosystems. Water Resour. Res. 54, 3409–3435. https://doi.org/10.1029/2017WR021357.

McShane, R.R., Driscoll, K.P., Sando, R., 2017. A review of surface energy balance models for estimating actual evapotranspiration with remote sensing at high spatiotemporal resolution over large extents. U. S. Geol. Surv. Sci. Inv. Rep. 2017–5087 19. https://doi.org/10.3133/sir20175087.

Morton, C.G., Huntington, J.L., Pohll, G.M., Allen, R.G., McGwire, K.C., Bassett, S.D., 2013. Assessing calibration uncertainty and automation for estimating evapotranspiration from agricultural areas using METRIC. J. Am. Water Resour. Ass. 49 (3), 549–562. https://doi.org/10.1111/jawr.12054.

Muñoz-Sabater, J., Dutra, E., Agustí-Panareda, A., Albergel, C., Arduninni, G., Balsamo, G., Boussetta, S., Choulga, M., Harrigan, S., Hersbach, H., Martens, B., Miralles, D.G., Piles, M., Rodríguez-Fernández, N.J., Zsoter, E., Buontempo, C., Thépaut, J.-N., 2021. ERA5-Land: a state-of-the-art global reanalysis dataset for land applications. Earth Syst. Sci. Data 13 (9), 4349–4383. https://doi.org/10.5194/essd-13-4349-2021.

Nieto, H., Kustas, W.P., Alfieri, J.G., Gao, F., Hipps, L.E., Los, S., Prueger, J.H., McKee, L. G., Anderson, M.C., 2019. Impact of different within-canopy wind attenuation formulations on modelling sensible heat flux using TSEB. Irr. Sci. 37, 315–331. https://doi.org/10.1007/s00271-018-0611-y.

Norman, J.M., Kustas, W.P., Humes, K.S., 1995. Source approach for estimating soil and vegetation energy fluxes in observations of directional radiometric surface temperature. Agric. Water Meteorol. 77 (3-4), 263–293. https://doi.org/10.1016/0168-1923(95)02265-Y.

Norman, J.M., Kustas, W.P., Prueger, J.H., Diak, G.R., 2000. Surface flux estimation using radiometric temperature - A dual-temperature-difference method to minimize measurement errors. Water Resour. Res. 36 (8), 2263–2274. https://doi.org/10.1029/2000WR900033.

Norman, J.M., Anderson, M.C., Kustas, W.P., French, A.N., Mecikalski, J., Torn, R., Diak, G.R., Schmugge, T.J., Tanner, B.C.W., 2003. Remote sensing of surface energy fluxes at 10^1-m pixel resolutions. Water Resour. Res. 39 (8), 1221. https://doi.org/10.1029/2002WR001775.

Pan, S., Pan, N., Tian, H., Friedlingstein, P., Sitch, S., Shi, H., Arora, V.K., Haverd, V., Jain, A.K., Kato, E., Lienert, S., Lombardozzi, D., Nabel, J.E.M.S., Ottlcé, C., Poulter, B., Zaehle, S., Running, S.W., 2020. Evaluation of global terrestrial evapotranspiration using state-of-the-art approaches in remote sensing, machine learning and land surface modeling. Hydrol. Earth Syst. Sci. 24, 1485–1509. https://doi.org/10.5194/hess-24-1485-2020.

Price, J.C., 1990. Using spatial context in satellite data to infer regional scale evapotranspiration. IEEE Trans. Geosci. Remote Sens. 28, 940–948. https://doi.org/10.1109/36.58983.

Saboori, M., Mokhtari, A., Afrasiabian, Y., Dacacche, A., Alaghmand, S., Mousivand, Y., 2021. Automatically selecting hot and cold pixels for satellite actual evapotranspiration estimation under different topographic and climatic conditions. Agr. Water Manag. 248, 106763. https://doi.org/10.1016/j.agwat.2021.106763.

Senay, G.B., Budde, M., Verdin, J.P., Melesse, A.M., 2007. A coupled remote sensing and simplified surface energy balance approach to estimate actual evapotranspiration from irrigated fields. Sensors 7 (6), 979–1000. https://doi.org/10.3390/s7060979.

Tasumi, M., 2019. Estimating evapotranspiration using METRIC model and Landsat data for better understandings of regional hydrology in the western Urmia Lake Basin. Agr. Water Manag. 226, 105805. https://doi.org/10.1016/j.agwat.2019.105805.

Timmermans, W.J., Kustas, W.P., Anderson, M.C., French, A.N., 2007. An intercomparison of the Surface Energy Balance Algorithm for Land (SEBAL) and the Two-Source Energy Balance (TSEB) modeling schemes. Remote Sens. Environ. 108 (4), 369–384. https://doi.org/10.1016/j.rse.2006.11.028.

Twine, T.E., Kustas, W.P., Norman, J.M., Cook, D.R., Houser, P.R., Meyers, T.P., Prueger, J.H., Starks, P.J., Wesely, M.L., 2000. Correcting eddy-covariance flux underestimates over a grassland. Agric. For. Meteorol. 103, 279–300. https://doi.org/10.1016/S0168-1923(00)00123-4.

United State Geological Survey (USGS), 2021. Landsat 8-9 Calibration and Validation (Cal/Val). Algorithm Description Document (ADD), version 4.0, p. 819. ⟨https://d9-wret.s3.us-west-2.amazonaws.com/assets/palladium/production/s3fs-public/atoms/files/LSDS-1747_Landsat8-9_CalVal_ADD-v4.pdf⟩ (Available at:).

Volk, J.M., Huntington, J.L., Melton, F.S., Allen, R., Anderson, M., Fisher, J.B., Kilic, A., Ruhoff, A., Senay, G.B., Minor, B., Morton, C., Ott, T., Johnson, L., Comini de Andrade, B., Carrara, W., Doherty, C.T., Dunkerly, C.W., Friedrichs, M., Guzman, A., Hain, C., Halverson, G., Kang, Y., Knipper, K., Laipelt, L., Ortega-Salazar, S., Pearson, C., Parrish, G.E., Purdy, A., ReVelle, P., Wang, T., Yang, Y., 2024. Assessing the accuracy of OpenET satellite-based evapotranspiration data to support water resource and land management applications. Nat. Water 2, 193–205. https://doi.org/10.1038/s44221-023-00181-7.

Webb, E.K., 1970. Profile relationships: the log-linear range, and extension to strong stability. Q. J. R. Meteorol. Soc. 96, 67–90. https://doi.org/10.1002/qj.49709640708.

Yang, Y., Su, H., Zhang, R., Tian, J., Li, L., 2015. An enhanced two-source evapotranspiration model for land (ETEML): Algorithm and evaluation. Remote Sens. Environ. 168, 54–65. https://doi.org/10.1016/j.rse.2015.06.020.

Yang, Y., Anderson, M.C., Gao, F., Hain, C.H., Semmens, K.A., Kustas, W.P., Noormets, A., Wynne, R.H., Thomas, V.A., Sun, G., 2017. Daily Landsat-scale evapotranspiration estimation over a forested landscape in North Carolina, USA, using multi-satellite data fusion. Hydrol. Earth Syst. Sci. 21 (2), 1017–1037. https://doi.org/10.5194/hess-21-1017-2017.

Zou, J., Lu, N., Jiang, H., Qin, J., Yao, L., Xin, Y., Su, F., 2022. Performance of air temperature from ERA5-Land reanalysis in coastal urban agglomeration of Southeast China. Sci. Total Environ. 828, 154459. https://doi.org/10.1016/j.scitotenv.2022.154459.